SUMMARY OF DLR RESULTS FROM THE SEVENTH AIAA DRAG PREDICTION WORKSHOP

Stefan Keye[1], Olaf Brodersen[1] & Stefan Melber-Wilkending[1]

[1]Dept. Transport Aircraft, Institute of Aerodynamics and Flow Technology, Lilienthalplatz 7, 38108 Braunschweig

Abstract

A summary of the German Aerospace Research Center's results from the seventh AIAA Computational Fluid Dynamics Drag Prediction Workshop held in Chicago, IL, 25-26 June 2022, is presented. The workshop had a focus on predicting the effect of shock-induced separation on the variation of lift and pitching moment with increasing angle-of-attack at transonic conditions and has used NASA's Common Research Model civil transport aircraft configuration as the reference geometry. DLR has contributed to five out of the six workshop test cases. These include a grid convergence study on the Wing-Body configuration (*Test Case 1a*), an angle-of-attack sweep using preset aero-elastic wing deflections obtained from a wind tunnel test (*Test Case 2a*), a Reynolds number sweep at constant lift coefficient (*Test Case 3*), and a coupled aero-structural simulation, where wing deflections are computed through a coupling to a computational structural analysis (*Test Case 6*).

Keywords: Drag Prediction Workshop, Computational Fluid Dynamics, Aero-Elasticity, Validation

Nomenclature

α	=	Angle-of-Attack
b	=	Wing Span
C_D	=	Drag Coefficient
C_L	=	Lift Coefficient
$C_{L,S}$	=	Sectional Lift Coefficient
C_{My}	=	Pitching Moment Coefficient
$C_{My,S}$	=	Sectional Pitching Moment Coefficient
c_{local}	=	Local Wing Chord
c_p	=	Static Pressure Coefficient
$c_{ref.}$	=	Reference Wing Chord
E	=	Young's Modulus
ε	=	Wing Twist Deformation
η	=	Nondimensional Spanwise Coordinate
i	=	CFD Face Centroid Index
j	=	CSM Grid Point Index
L	=	Grid Level
Ma_∞	=	Freestream Mach Number
N_P	=	Number of Grid Points
N_E	=	Number of Grid Elements
N_{BL}	=	Number of Grid Boundary Layers
q	=	Dynamic Pressure
Re	=	Reynolds Number
s	=	Wall Normal Stretching Ratio
$T_{ref.}$	=	Reference Temperature
u, v, w	=	Cartesian Deflection Components
x	=	Streamwise Cartesian Coordinate
y	=	Lateral Cartesian Coordinate
Δy_1	=	First Cell Height
y^+	=	Normalized Wall Distance
z	=	Vertical Cartesian Coordinate

1. Introduction

The accurate calculation of aerodynamic forces and moments is of significant importance during the design and analysis of an aircraft configuration. Over the last two decades, the field of Reynolds-averaged Navier-Stokes (RANS) based Computational Fluid Dynamics (CFD) has significantly progressed regarding robustness, accuracy, efficiency, and the capability to handle complex configurations [1, 2]. Today, incremental aerodynamic coefficients of typical transonic aircraft can be calculated with acceptable accuracy, both around the cruise design point and for non-separated flows in general. However, regarding absolute values and increments at off-design conditions, significant challenges still exist to accurately compute aerodynamic data and model the underlying complex flow physics.

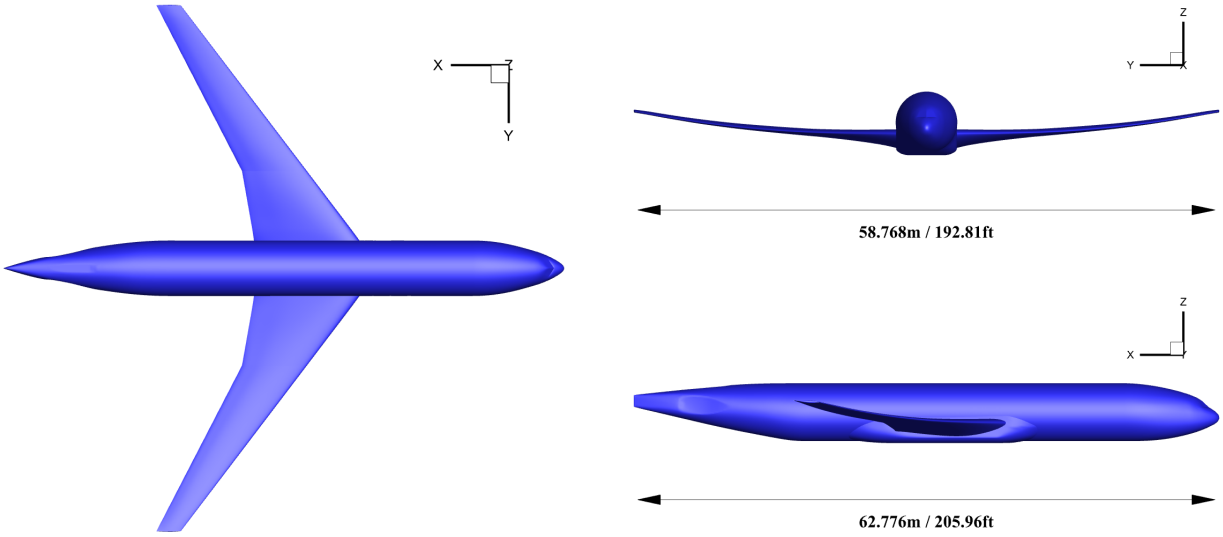

Figure 1 – NASA Common Research Model in Wing-Body configuration.

Based on these challenges, a working group of the AIAA Applied Aerodynamics Technical Committee initiated the CFD Drag Prediction Workshop (DPW) series[1] in 2001, resulting in seven international workshops to date. Participants and committee results have been summarized in numerous papers [3, 4, 5, 6, 7, 8, 9]. Currently (as of May 2024), the 8th workshop, wich will be held in collaboration with the 4th Aeroelastic Prediction Workshop in 2026, has entered the planning process. For details and updates please refer to the DPW website.
Starting from DPW-4, the NASA Common Research Model (CRM) civil transport aircraft configuration, Figure 1, designed by NASA's Subsonic Fixed Wing Technical Working Group and Vassberg et al. [22], has been used as the reference geometry. Geometrical and experimental data of the model are found on the NASA CRM website[2].
DLR's Institute of Aerodynamics and Flow Technology is supporting DPW as a committee member, e.g. through the activities associated with the preparation of the DLR-F6 wind tunnel model for testing in NASA Langley's National Transonic Facility (NTF) for DPW-3 [10], the investigation of aeroelastic effects on the CRM wind tunnel model [11], or the development of deformed CRM CAD geometries for DPW-6 [12] and DPW-7 [13], and as a participant [14, 15, 16, 17, 18, 19, 20, 21].
The 7th workshop had an emphasis on shock-induced separation, including Reynolds number effects, grid adaptation, and unsteady solution technologies. Additionally, following observations from the the 4th to 6th workshops, aero-elastic studies were included. Test cases comprize six series of computations[3]. At DLR the Institute of Aerodynamics and Flow Technology has contributed to the following four test cases:

1. *Test Case 1a*, CRM Wing-Body Grid Convergence Study, Re = 20M [Required]:
   - Calculate grid convergence, using at least 4 grids out of the 6-member baseline grid family.
   - Flow conditions: $Ma_\infty = 0.85$; $Re = 20.0 \cdot 10^6$; $T_{ref.} = 116.48$K; $C_L = 0.5800 \pm 0.0001$.
2. *Test Case 2a*, CRM Wing-Body Alpha Sweep, Re = 20M [Required]:
   - Conduct angle-of-attack sweep, using 'LoQ' aero-elastic deflections measured in ETW Wind Tunnel Test.
   - Flow conditions: $Ma_\infty = 0.85$; $Re = 20.0 \cdot 10^6$; $T_{ref.} = 116.48$K; $C_L = 0.5000 \pm 0.0001$ and angle-of-attack sweep = [2.75, 3.00, 3.25, 3.50, 3.75, 4.00, 4.25] degrees.

[1] http://aiaa-dpw.larc.nasa.gov/
[2] http://commonresearchmodel.larc.nasa.gov/
[3] https://aiaa-dpw.larc.nasa.gov/Workshop7/Case_defnI.pdf

3. *Test Case 3*, CRM Wing-Body Reynolds Number Sweep At Constant CL [Required]:
   - Flow conditions: $Ma_\infty = 0.85$; $C_L = 0.5000 \pm 0.0001$; $Re = 5.0 \cdot 10^6/T_{ref.} = 310.93$K; $Re = 20.0 \cdot 10^6/T_{ref.} = 116.48$K; $Re = 20.0 \cdot 10^6/T_{ref.} = 154.26$K; $Re = 30.0 \cdot 10^6/T_{ref.} = 116.48$K.
4. *Test Case 6*, CRM Wing-Body Coupled Aero-Structural Simulation [Optional]:
   - Fixed lift condition and/or angle-of-attack sweep, coupled with computational structural analysis.
   - static aero-elastic deflections calculated, starting from the undeformed 'NoQ' geometry.
   - Flow conditions: $Ma_\infty = 0.85$; $Re = 20.0 \cdot 10^6$; $T_{ref.} = 116.48$K; $C_L = 0.5800 \pm 0.0001$ and/or angle-of-attack sweep = [3.25, 3.50, 3.75, 4.00, 4.25] degrees.

2. Numerical Simulations

2.1 CAD Geometries

During DPW-5 a significant influence of wind tunnel model wing deformations on both the overall aerodynamic coefficients and wing static pressure distributions was found. An investigation of aeroelastic effects of the CRM [23] revealed that varying flow conditions, e.g. angle of attack, Mach number, or Reynolds number, and the associated variation of aerodynamic loads and corresponding model deformations caused a degradation in the correlation between numerical and experimental results. In order to avoid this degradation, a set of deformed CRM CAD geometries was provided by the DPW Organizing Committee for the test cases defined for DPW-7. The deformations are based on experimental wing deflection measurements on the CRM, performed during the Trans National Access (TNA) test campaign at the European Transonic Wind Tunnel (ETW) in Cologne, Germany, in 2014 [24]. The CAD geometries provided for DPW-7 include two sets of wing deformations for $\alpha = [2.50, 2.75, \ldots, 4.25]^\circ$, one using a low ratio of dynamic pressure versus Young's modulus $q/E = 0.3260$, labeled as 'LoQ', and a second one for a high $q/E = 0.4936$, referred to as 'HiQ'. Details on the process developed to derive the aeroelastically deformed CAD geometries are described in Ref. [13].

2.2 Computational Grids

DLR's custom-built unstructured, hybrid CFD grids were generated using the grid generation package SOLAR V15.3.8 [25]. For the boundary layer mesh, SOLAR primarily uses hexahedra-type elements, while, the farfield mesh is built from tetrahedral elements. Grids were generated for *Test Cases 1a*, *2a*, and *6*, and provided as common grids on the DPW-7 website[4] for free usage by workshop participants. All grids were generated for a boundary layer resolution of $Re = 30.0 \cdot 10^6$.

Test Case 1a requires a baseline grid family, consisting of six mesh levels $L = [1, \ldots, 6]$ with a size factor of $[(L+2)/(L+1)]^3$ in terms of total number of points between consecutive levels[5]. The values specified for Δy_1 lead to $y^+ \approx 1$ for the flow conditions defined in Section 1. Six grid levels with spatial resolutions ranging from *Tiny* ('T') up to *Ultra Fine* ('U') were generated on the CRM geometry with '3.00deg LoQ' aeroelastic wing deflection. For *Test Case 2a* a series of eight *Medium* sized grids are required on wing geometries with 'LoQ' aeroelastic deflections for angles-of-attack between 2.50deg and 4.25deg in increments of 0.25deg. These grids were generated by applying the control source setup for the *Medium* grid from *Test Case 1a* to each of the eight wing geometries. Similarly, the *Medium* baseline grid for *Test Case 6* was generated on the undeformed ('NoQ') geometry.

Using DLR's standard best practice settings for element size distribution between leading and trailing edges a *Fine* mesh ('F') for *Test Case 1a* was setup as a starting point. By adjusting the global source scaling of that mesh, it was sized to approximately meet the point number specified in the gridding guidelines. Based on this initial mesh all other family members were created by proportionally scaling all mesh density control sources by the factor $(L+2)/(L+1)$.

The basic procedure for generating the meshes starts with the quad-dominant surface mesh generation. Non-isotropic quadrilateral elements allow for an efficient discretization of single-curvature

[4] https://dpw.larc.nasa.gov/DPW7/DLR_Grids.REV00/

[5] https://aiaa-dpw.larc.nasa.gov/Workshop7/DPW-7_baselineGridFamilyPlanRevB.pdf

surfaces, such as wing leading edges. A quadrilateral surface mesh enables the generation of elements with higher aspect ratios than this is recommended with triangles, while maintaining or even reducing discretization errors for a given number of mesh points. The amount of triangular surface elements is typically in the order of 0.5% of the total number of surface elements.
The boundary layer mesh is created by extruding the surface mesh in normal direction from the viscous wall surfaces into the computational domain. Due to the quad-dominant mixed element surface mesh, the advancing layer step is consistently hexahedra-dominant, with some triangle-based prismatic layer stacks, where needed. Pyramidal elements are used to achieve a conformal interface between the near-field advancing-layer mesh and the farfield advancing-front mesh. According to the DPW-7 gridding guidelines the first wall distance Δy_1 is changing with mesh resolution level, Table 1, wall normal stretching of the cells, however, remains constant at $s = 1.2$. Because SOLAR determines the maximum number of boundary layers by element height-to-width ratio, the number of layers also is essentially constant ($N_{BL} = 52 \ldots 53$, cf. Table 1).
The remaining field volume is filled with tetrahedra. To capture the gradients of the resulting flow, especially possible shocks on the wing upper side, this region around the wing is refined locally.
Figure 2 shows the quad-dominant surface mesh in the leading (a) and trailing (b) edge regions at the wing root. The boundary layer grid is represented by cut planes (shown in orange).

Table 1 – Overview of computational grids family for *Test Case 1a*.

Level	**Name**		$N_P/10^6$	$N_E/10^6$	Δy_1 / **[μm]**	N_{BL}
1	*Tiny*	('T')	11.699	31.589	6.560	53
2	*Coarse*	('C')	25.008	64.335	4.374	53
3	*Medium*	('M')	47.065	130.75	3.280	52
4	*Fine*	('F')	76.508	224.10	2.624	52
5	*Extra Fine*	('X')	118.86	367.93	2.187	52
6	*Ultra Fine*	('U')	164.53	534.17	1.874	53

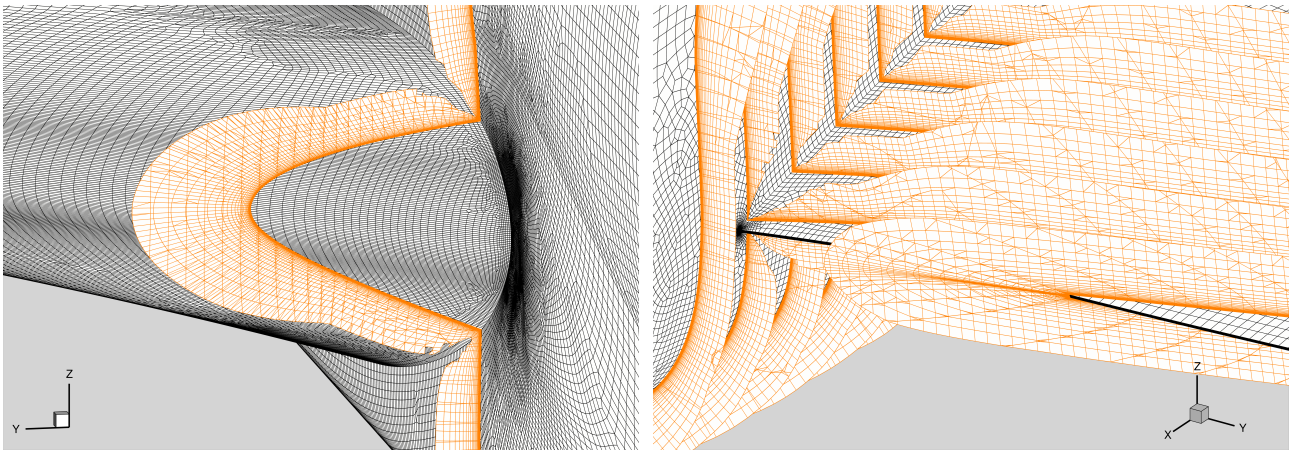

(a) *Leading Edge* (b) *Trailing Edge*

Figure 2 – Chopping of the SOLAR boundary layer grid in the wing-fuselage junction, *Medium* grid level.

2.3 Flow Solver

The Reynolds-averaged Navier-Stokes solver TAU has been developed at DLR starting in the mid 1990's. The code originates from the German CFD project MEGAFLOW [26, 27, 28], which has integrated developments of DLR, aircraft industry, and universities. Today, the software package is continuously upgraded and expanded by the institutes $C^2A^2S^2E$ (Center for Computer Applications

in AeroSpace Science and Engineering) department and is used by DLR and European partners in industry, research, and academia.
TAU is an edge-based, cell-vertex, finite volume, unstructured solver, which uses the dual grid technique and fully exploits the advantages of hybrid grids. The numerical scheme is based on the finite volume method and provides different spatial discretization schemes, like upwind and central [28]. The central scheme is of second order accuracy and employs the Jameson-type of artificial dissipation in scalar and matrix mode [29, 30]. Time integration is performed using both, the explicit Runge-Kutta multi-stage, and the Lower-Upper Symmetric Gauss-Seidel (LU-SGS) schemes. TAU has been developed with a particular focus on industrial aeronautical applications, thus providing advanced techniques, like overlapping grids for treating unsteady phenomena, and complex geometries. A detailed description of TAU is provided in Ref. [28].

2.4 Turbulence Models

CFD simulations for DPW-7 were run using the linear, one-equation, negative Spalart-Allmaras eddy viscosity turbulence model [31] (SA-neg), the SA model with the Quadratic Constitution Relation extension [32] applied (SA-QCR), and the Speziale-Sarkar-Gatski/Launder-Reece-Rodi differential Reynolds stress model with length-scale correction [33] (RSM-ln(ω)).

3. Results

3.1 Test Case 1a - Grid Convergence Study, $Re = 20.0 \cdot 10^6$

3.1.1 Aerodynamic Coefficients

Figure 3 shows the convergence of overall aerodynamic parameters with grid size factor $N_P^{-2/3}$ for the three turbulence models used in *Test Case 1a*. The dash-dotted lines represent a Richardson extrapolation, which applies a standard 2^{nd} order least squares fit. For 2^{nd} order codes the results should be linear versus grid size factor. Interceptions with the y-axis provide an estimate for the theoretical infinite resolution, i.e. the continuum results.
All computations fall within the required lift accuracy limits of $C_L = 0.5800 \pm 0.0001$, Figure 3(a), but without any clear tendencies regarding grid size.
As the test case requires $C_L = const.$, angle-of-attack is used here for total lift convergence assessment, Figure 3(b). For all three turbulence models angle-of-attack increases with grid size by $\Delta\alpha \approx +0.025^\circ$ at the same rate from the *Tiny* to the *Ultra Fine* grid with good linearity. Differences in angles-of-attack at the extrapolated continuum solutions were found to be small at $\Delta\alpha = +0.033^\circ$ between the two SA models, and $\Delta\alpha = +0.049^\circ$ between SA-QCR and RSM-ln(ω), respectively.
Figure 3(c) shows convergence of overall drag coefficient C_D, based on a fully turbulent CFD simulation. Again, linearity with grid size is good for all turbulence models, with drag values decreasing by approximately $\Delta C_D = -3.5$ drag counts from the coarsest to the finest grids. Differences between turbulence models remain small, with the SA models predicting the lowest values of $C_D = 269.9$d.c. (SA-neg) and $C_D = 271.4$d.c. (SA-QCR) at continuum, while a marginally higher value of $C_D = 274.6$d.c. is computed with RSM-ln(ω). Variations of total drag are partially caused by turbulence modeling, but are mainly due to the differences in angles-of-attack computed for this constant-lift case.
The variation of pitching moment coefficient C_{My} as a measure of overall surface pressure distribution is plotted in Figure 3(d). Differences between the turbulence models are comparatively small. Negative values occur due to the lack of a horizontal stabilizer on the CRM configuration under investigation. The 'nose down' action is reduced with grid size for all turbulence models, where the gradient for RSM-ln(ω) is steeper by a very small amount than for the SA models.
In summary, the deviations between overall aerodynamic coefficients with respect to both mesh sizes and turbulence modeling were found to be exceptionally small, which will be confirmed by the more detailed investigation of wing static pressure distributions in the next section.

3.1.2 Wing Static Pressure Distributions and Sectional Aerodynamic Coefficients

The chordwise distribution of wing static pressure coefficient is plotted in Figure 4 for all six grid levels and two selected turbulence models. Two representative spanwise sections, one on the inboard wing at $\eta = 0.3971$ and the other on the outboard wing at $\eta = 0.9500$, were selected for comparison.

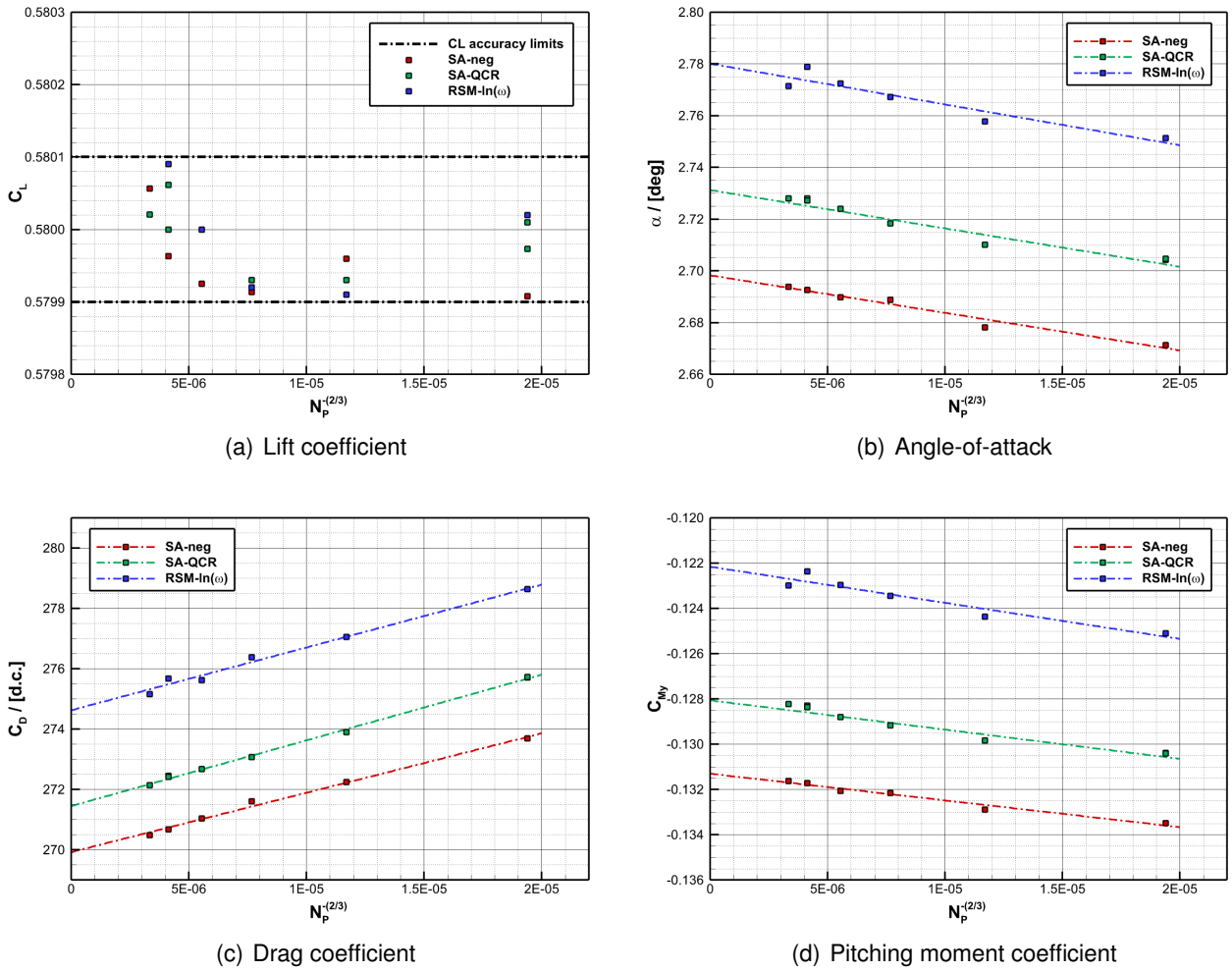

(a) Lift coefficient

(b) Angle-of-attack

(c) Drag coefficient

(d) Pitching moment coefficient

Figure 3 – Grid convergence for three different turbulence models.

Variations between mesh levels are found to be very small on the inboard wing, while on the outboard wing shock location is shifting upstream with increased mesh resolution. The effect is somewhat stronger for the RSM-ln(ω) model than for SA-neg. Still, the influence on sectional lift and pitching moment, Figure 5, remains very small, which confirms the previously observed weak effect of mesh resolution on the globall aerodynamic coeficients.

Similar results are found when comparing pressure distributions for all turbulence models, Figure 6. Here, the *Tiny* and *Extra Fine* grid levels are used for comparison. For both mesh levels some very minor differences may be recognized on the inboard wing sections. On the outboard wing shock location shifts upstream from SA-neg to RSM-ln(ω), which leads to minor differences of sectional lift and pitching moment coefficients in that area of the wing, Figure 7, and is consistent to the reduction of overall pitching moment, Figure 3(d). The upstream shift in shock location rather is related to the increasing angles-of-attack, cf. Figure 3(b), than to turbulence model properties. Again, the influence of the applied turbulence model on overall lift is found to be largely insignificant.

3.1.3 Side-of-Body Separation

Finally, the influence of both grid size and turbulence modelling on the size of the side-of-body (SoB) separation, which frequently is observed at the Wing-Body intersection close to the trailing edge, was investigated. It should be noted that the geometrical determination of the SoB separation bubble size requires a manual inspection of surface streamlines and therefore the data should be considered ambiguous to some extent. Figure 8 shows an example of SoB development with grid size for the SA-neg model, spanwise separation extension for all turbulence models is plotted in Figure 9. For each turbulence model separation size almost vanishes for the *Tiny* grid and increases with grid level

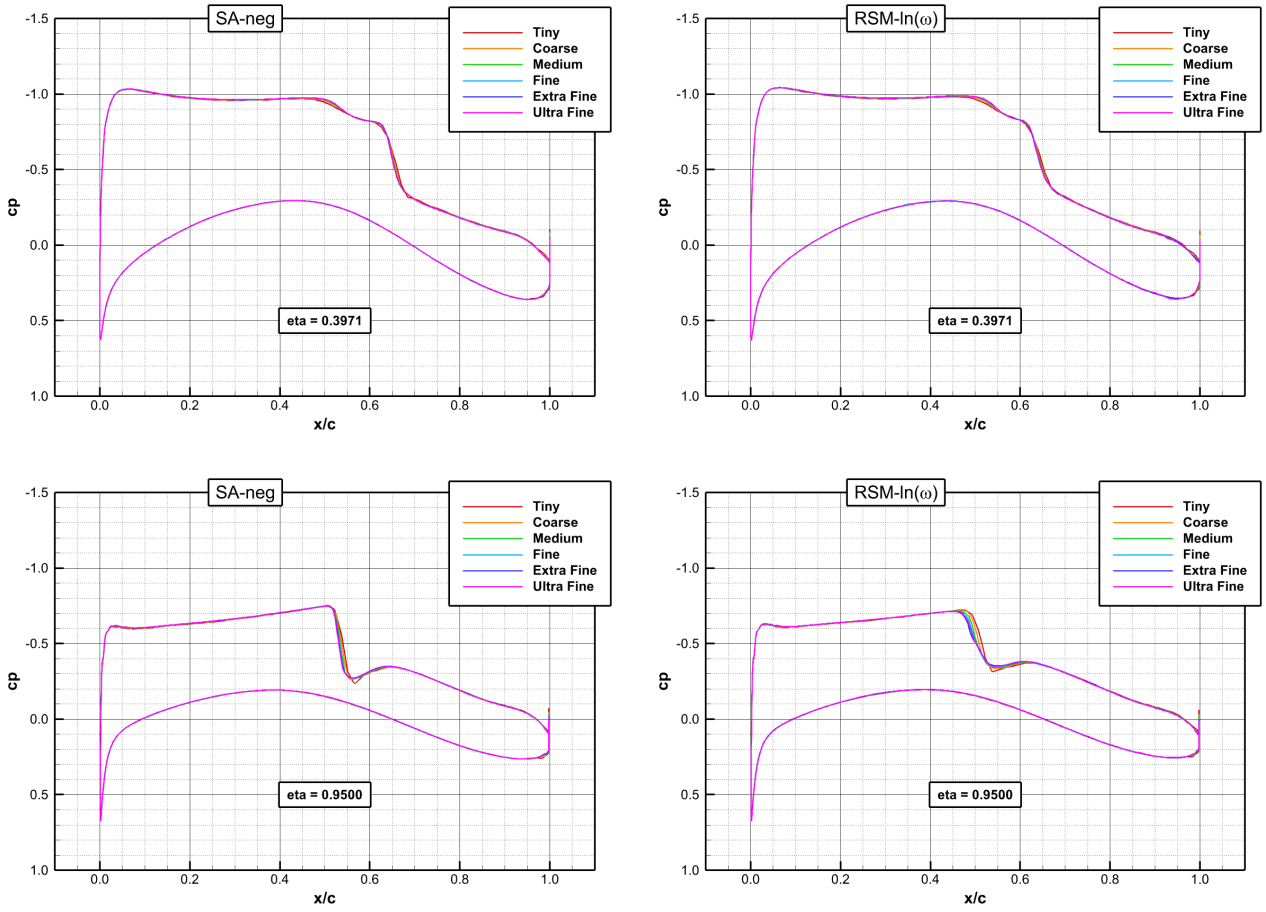

Figure 4 – Comparison of wing static pressure distributions for all mesh levels.

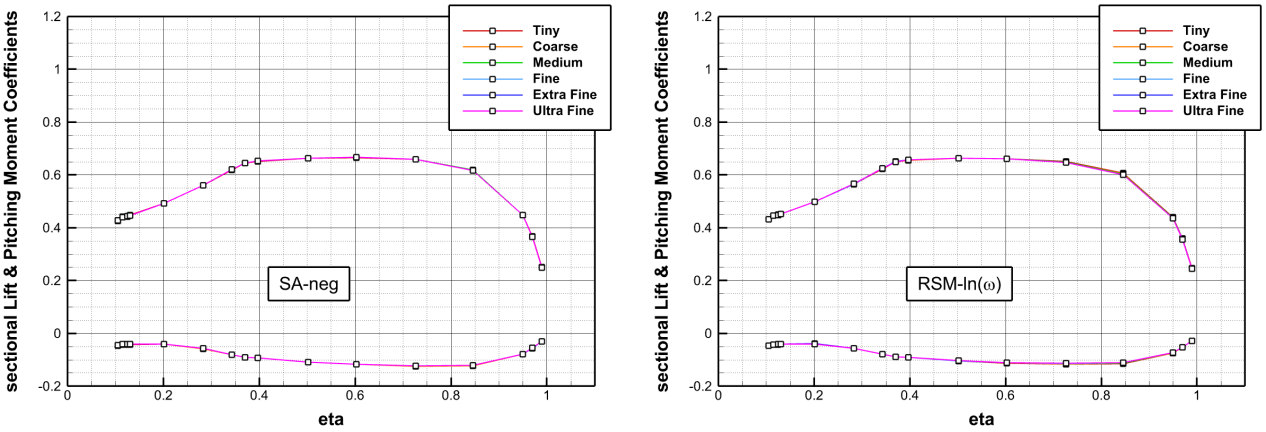

Figure 5 – Sectional lift (upper curves) and pitching moment (lower curves) coefficients for all mesh levels.

with spanwise extension converging with higher grid levels. Generally, an increasing separation size should cause a reduction of lift. However, overall separation size at the given flow conditions is too small for the effect to become visible in the spanwise lift distributions, Figures 5 and 7. As a result, an influence of the separation sizes found on the SOLAR grids on overal lift prediction can be neglected.

3.2 Test Case 2a - Alpha Sweep, $Re = 20.0 \cdot 10^6$

This test case is based on an angle-of-attack sweep to investigate CFD predictions in a range where significant flow separation is expected. This flight regime is of particular importance to determine

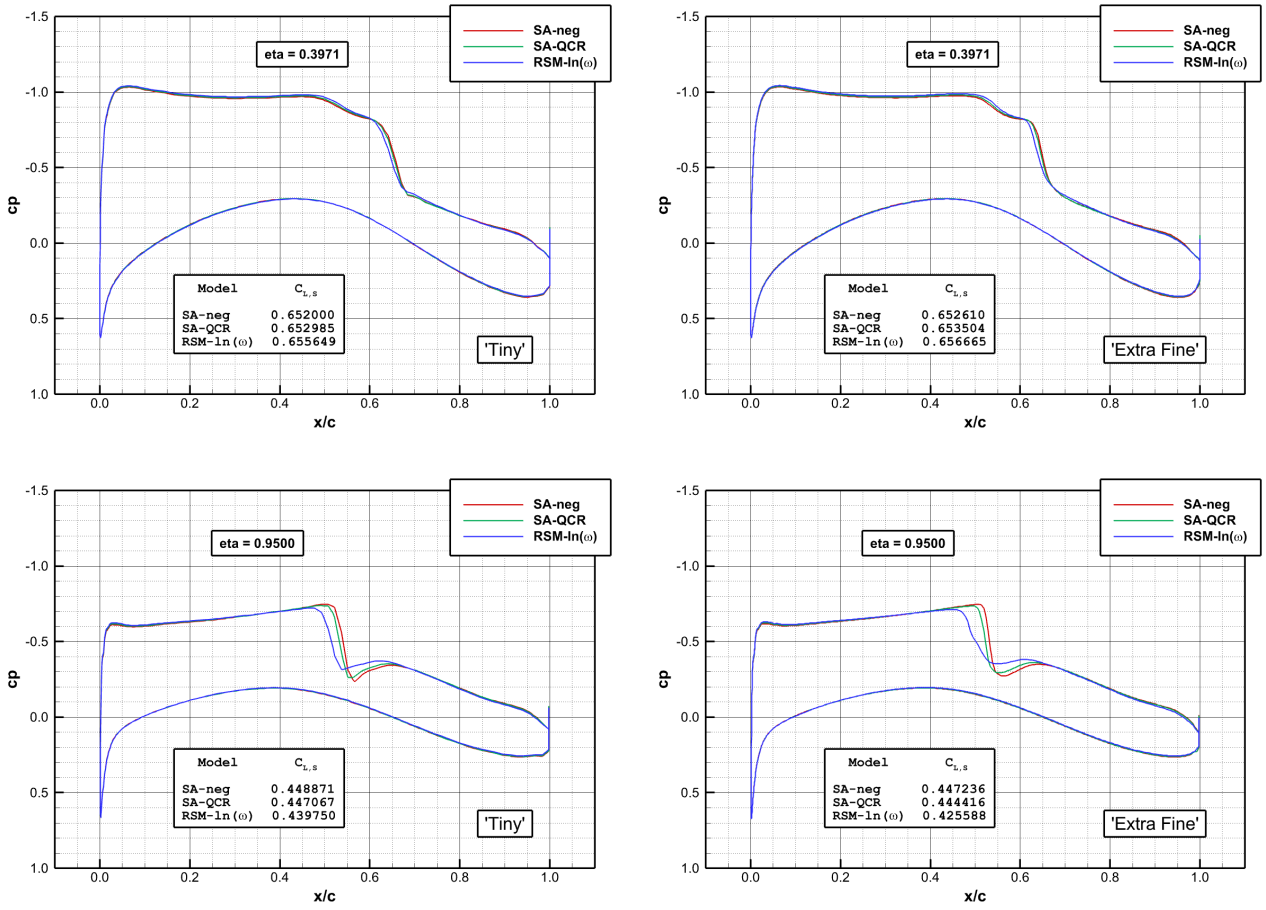

Figure 6 – Comparison of wing static pressure distributions for all turbulence models.

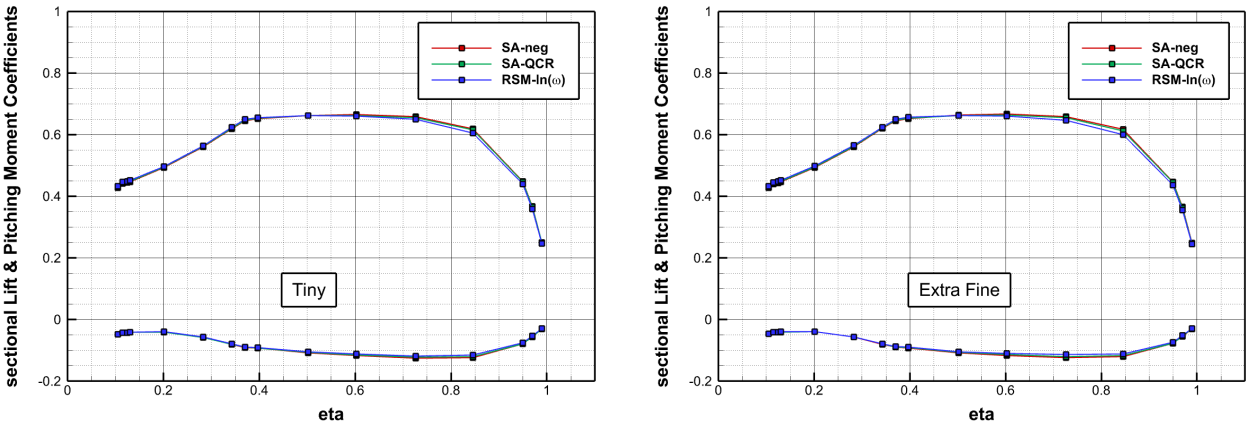

Figure 7 – Sectional lift (upper curves) and pitching moment (lower curves) coefficients for all turbulence models.

aerodynamic loads as well as stability and control characteristics. Eight angles-of-attack were specified between $\alpha = 2.50^\circ$ and $\alpha = 4.25^\circ$ in increments of $\Delta\alpha = 0.25^\circ$. In order to account for the static aeroelastic deformation of the wind tunnel model, a separate geometry was defined for each angle-of-attack requested.

In Figure 10 the variations of lift and pitching moment coefficient, along with the NTF test data are shown for the SA-neg and RSM-ln(ω) turbulence models, respectively. Compared to the test data, solutions for both turbulence models indicate higher lift values over the entire angle-of-attack range and more negative, i.e. nose down, pitching moment for given lift coefficients. The offset in pitching

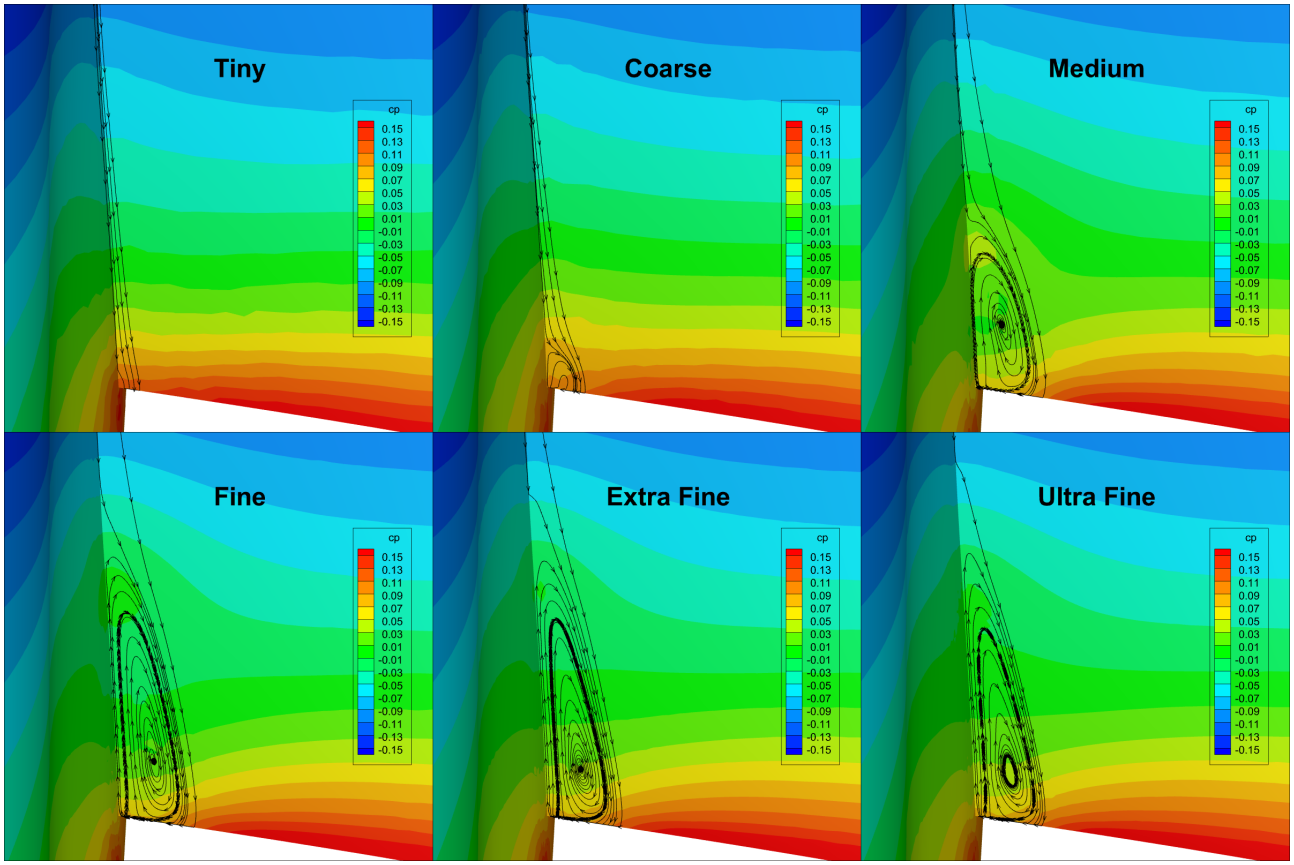

Figure 8 – Example of SoB separation development with grid size (Turbulence Model: SA-neg).

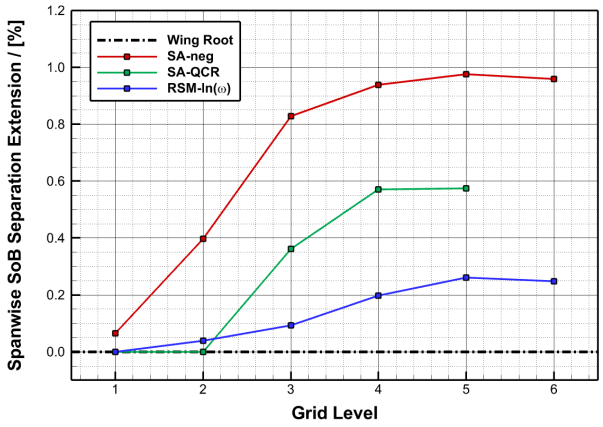

Figure 9 – Spanwise SoB extension for all turbulence models.

moment is partially due to the fact that the tail sting used as a wind tunnel model suspension is not included in the CFD geometry. In the static pressure distributions, Figure 11, the computed shock locations on the outboard wing lie downstream of the measurements. This is consistent to the observed deviations in both lift and pitching moment. Results for the RSM-ln(ω) model show a large upstream shock displacement with increasing angle-of-attack, Figure 11(d) to 11(f), leading to a stronger pitch break than compared to the SA-neg model.

The discontinuous decrease in lift for SA-neg from $\alpha = 3.75^\circ$ to $\alpha = 4.00^\circ$ is caused by the sudden growth of the SoB separation, Figure 12. The effect of the separation also becomes visible in the inboard static pressure distribution, Figure 11(c). The occurance of the separation is a purely numerical effect, caused by the one-equation turbulence model that, unlike the RSM-ln(ω) model, does not take into account the non-isotropic turbulent shear stresses in the corner flow along the Wing-Body

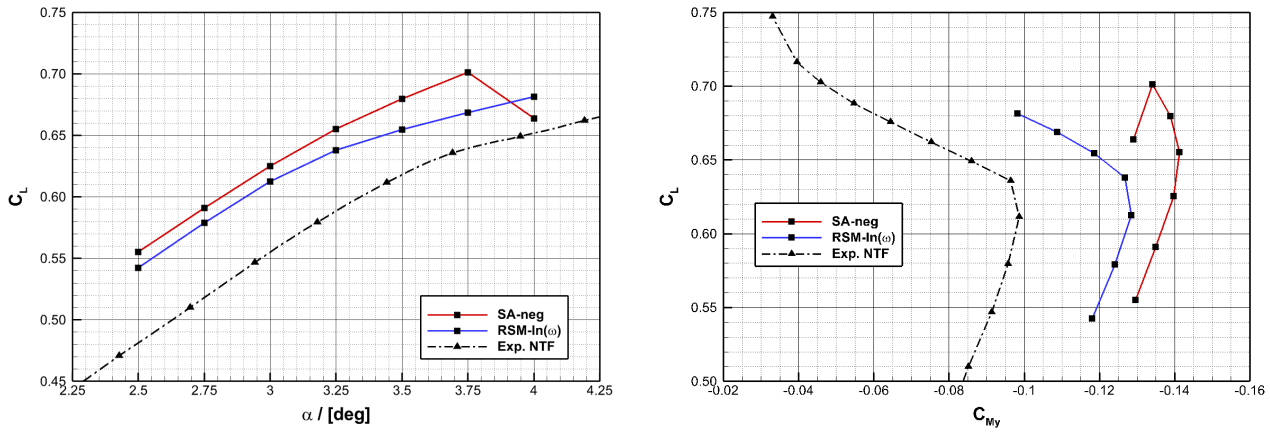

(a) Lift vs. angle-of-attack

(b) Lift vs. pitching moment

Figure 10 – Polar results.

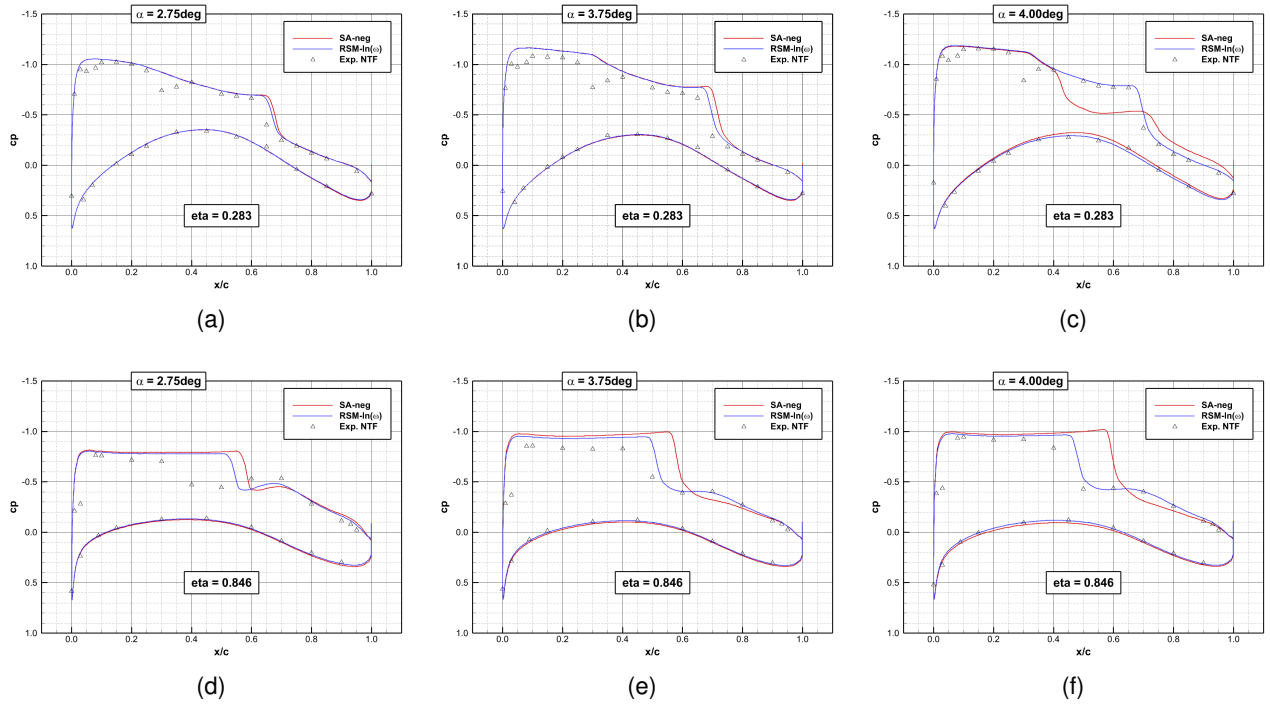

(a) (b) (c)

(d) (e) (f)

Figure 11 – Static pressure distributions on inboard and outboard wing for different angles-of-attack.

intersection. In the wind tunnel data no evidence of flow separation at the wing root is found in the static pressure distributions or lift curves.

For a complete assessment of the results it should be kept in mind that the overall differences between CFD simulations and test data could partially be due to the missing mounting system corrections in the experimental data.

3.3 Test Case 3 - Reynolds Number Sweep At Constant C_L

In this test case a Reynolds number sweep at constant lift coefficient $C_L = 0.5000 \pm 0.0001$, representative for a cruise condition, is performed. Unfortunately, due to technical limitations of the cryogenic wind tunnels, it was not possible to run the complete sweep from $Re = 5.0 \cdot 10^6$ to $Re = 30.0 \cdot 10^6$ at a constant dynamic pressure. The $Re = 5.0 \cdot 10^6$ and first $Re = 20.0 \cdot 10^6$ conditions were measured at a low dynamic pressure ('LoQ'), and the second $Re = 20.0 \cdot 10^6$ and $Re = 30.0 \cdot 10^6$ conditions were recorded at a high dynamic pressure ('HiQ').

Reynolds number increments are shown in Figure 13 for the 'LoQ' and 'HiQ' conditions. CFD results

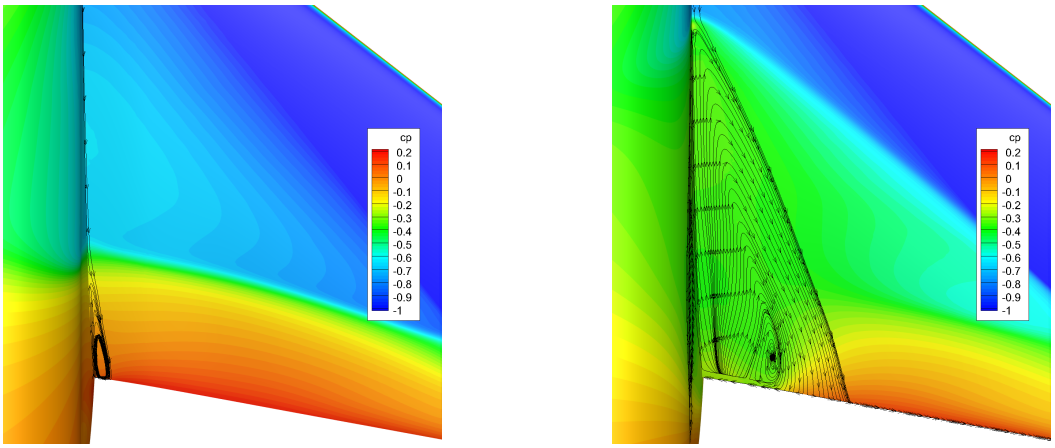

(a) $\alpha = 3.75°$ (b) $\alpha = 4.00°$

Figure 12 – Development of SoB separation for SA-neg at high angles-of-attack.

are compared to experimental data from two wind tunnel campaigns, in NTF for the Wing-Body configuration, and in ETW for the Wing-Body-Tail configuration. It is assumed that the presence of the tail does not affect the increments at the given flow condition.
The computed increments are consistent with respect to both the overall tendency and magnitude. The expected gain in lift with increased Reynolds number due to reduced boundary layer displacement thickness is correctly captured. For the 'HiQ' condition both lift and drag increments are considerably smaller due to the smaller Reynolds number ratio. The agreement between CFD and ETW results is considerably better than for NTF. This is likely due to the sting correction that has been applied to the ETW data. Differences between turbulence models are small because of the noncritical flight state without flow separation.

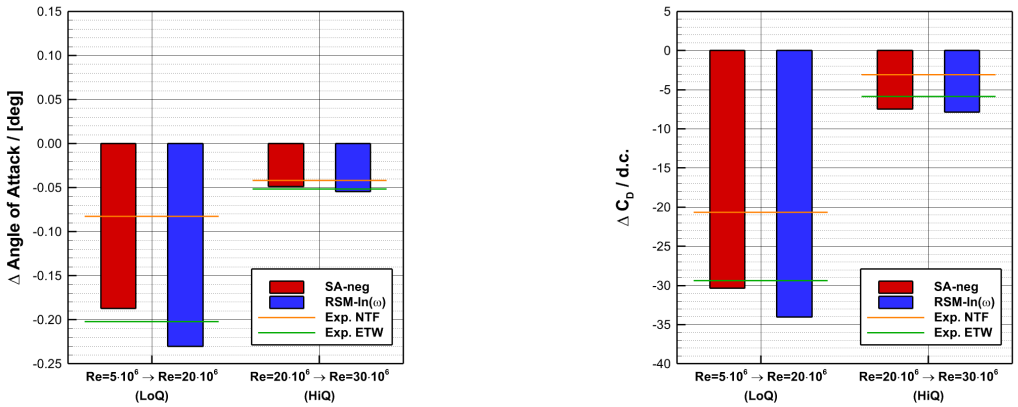

(a) Angle-of-attack (b) Total drag

Figure 13 – Influence of Reynolds number on angle-of-attack and drag.

3.4 Test Case 6 - Coupled Aero-Structural Simulation

3.4.1 Fluid-Structure-Coupled Simulation Procedure

DLR's fluid-structure interaction (FSI) simulation procedure, Figure 14, is based on a direct coupling of high-fidelity CFD and computational structural mechanics (CSM) methods [34]. The simultaneous interaction between outer flow field and flexible aircraft structure is modeled through alternately solving the Reynolds-averaged Navier-Stokes equations and the basic equations of structural mechanics, and the interpolation of aerodynamic forces and structural deflections over the common surface of CFD and structural domains. For the investigations described here, DLR's in-house flow solver TAU

and the commercially available structural analysis code NASTRAN® [35] were used. DLR's FSI simulation approach has been validated using a variety of test cases and flow conditions, including both wind tunnel [36, 19, 23, 37, 38] and flight test data [39, 40, 41, 42].

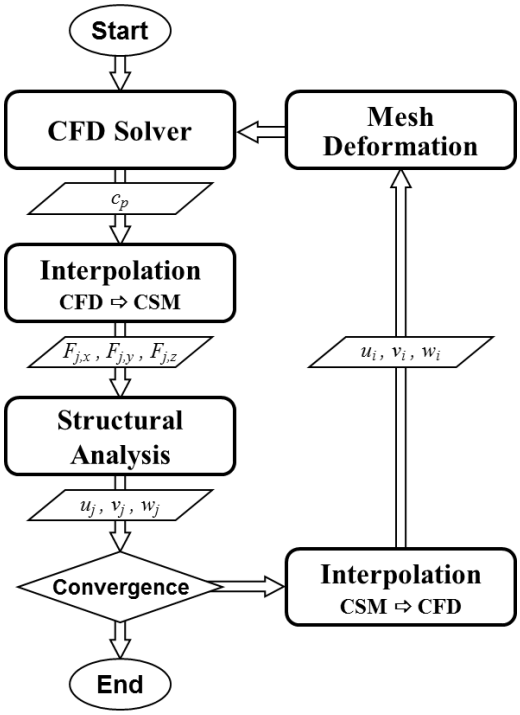

Figure 14 – Numerical simulation procedure for aero-elastic analyses.

3.4.2 Results

In Figures 15 and 16 the chordwise distributions of static pressure coefficient using the *Medium* baseline 'NoQ' grid and RSM-ln(ω) turbulence model are plotted at $C_L = 0.58$ and $\alpha = 4.00°$, respectively, and for two spanwise sections, at $\eta = 0.1306$ with neglectable wing deformation, and at $\eta = 0.8456$, where large wing deformations occur. Results are compared to experimental data from the Trans National Access (TNA) test campaign at the European Transonic Wind Tunnel (ETW) in Cologne, Germany, in 2014 [24].

An overall good agreement is found for both flow conditions and on both wing sections between the fully-coupled aeroelastic simulation and measured data. At $C_L = 0.58$ rooftop pressure level on the outboard wing section is slightly lower for the coupled simulation, compared to the experiment. For both flow conditions shock locations on the outboard wing sections appear to be predicted somewhat downstream of the experiment. However, the limited chordwise resolution of pressure taps does not allow for a precise determination of shock position in the measured data.

Figure 17 shows an example of spanwise wing bending (a) and twist (b) distributions in comparison to ETW deformation data at $C_L = 0.58$. It should be kept in mind that all deformations shown here relate to the wind tunnel model scale which is 2.7% of the full-size CRM. Bending deflections, Figure 17(a), reveal a very good agreement to measured data, with a maximum deviation of $\Delta w = -0.308$mm at wing tip. For the aerodynamically more relevant twist deformation, Figure 17(b), a maximum deviation of $\Delta\varepsilon = +0.0715$deg occurs, also at wing tip. Although the computed twist shows minor deviations from the measured course progression, the prediction error lies within the measurement accuracy, indicated by black error bars, over the entire span and therefore is concidered reasonably accurate. Similar results were found for all other angles-of-attack where experimental data is available.

In Figure 18 bending (a) and twist (b) deflections at wing tip are plotted over angle-of-attack. Bending deviations from measured data increase from $\Delta w = -0.22$mm (1.33%) at $\alpha = 2.50$deg to $\Delta w = +0.33$mm (1.61%) at $\alpha = 4.00$deg. Twist predictions are generally smaller by arround 5% than measured values, but remain within the experimental margin of error over the entire angle-of-attack range. Based on the limited information available it is assumed that the discrepancies between numerical

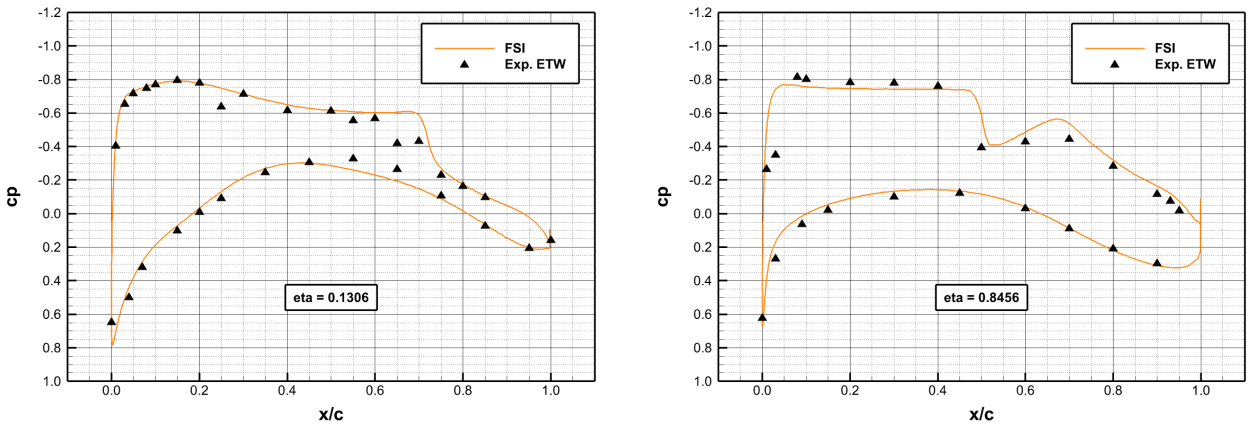

Figure 15 – Comparison of wing static pressure distributions, $C_L = 0.58$.

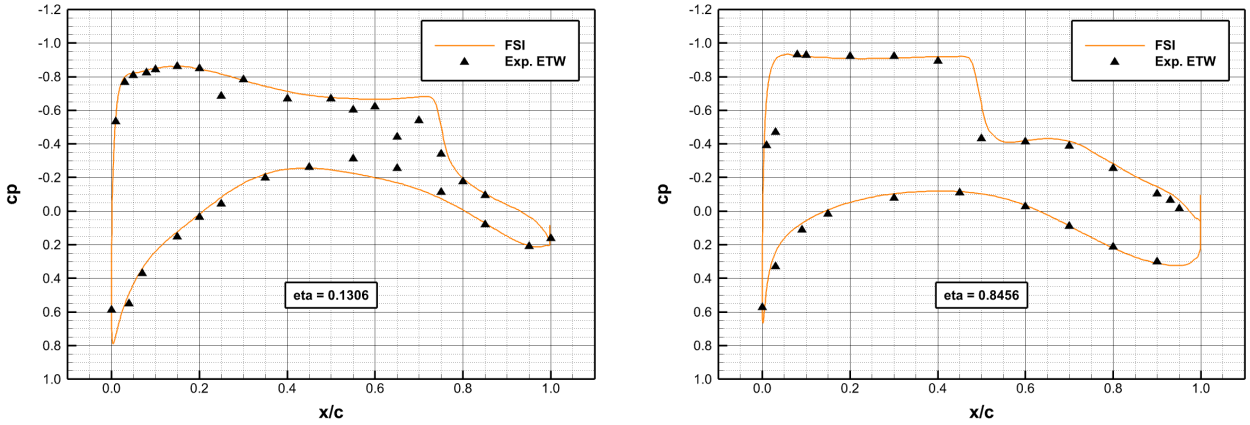

Figure 16 – Comparison of wing static pressure distributions, $\alpha = 4.00°$.

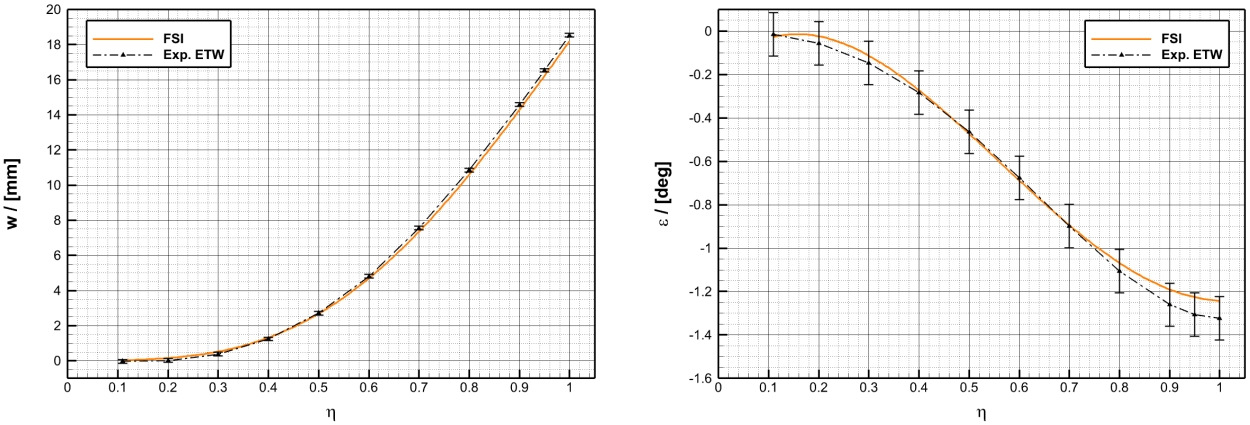

(a) Bending (b) Twist

Figure 17 – Comparison of computed and measured wing bending and twist deformation, $C_L = 0.58$.

simulation and experiment are partially caused by differences in wing stiffness between the finite-element structural model and the actual wind tunnel structure due to manufacturing tolerances, and experimental errors, in particular when measuring the very small deflection differences associated with twist deformations.

Still, the results obtained for *Test Case 6* demonstrate that DLR's aeroelastic simulation method is capable of correctly predicting aerodynamic coefficients, pressure distributions, and wing defor-

mations for varying flow conditions. The major advantage over conventional CFD methods is the independence from preliminary deformation measurements, which otherwise need to be obtained in expensive wind tunnel experiments and usually are not performed by default.

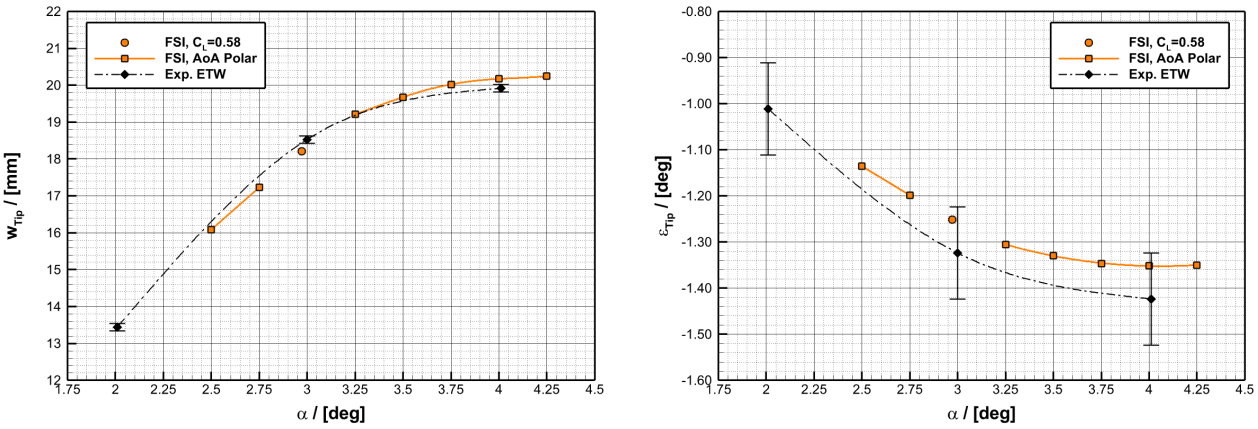

(a) Bending (b) Twist

Figure 18 – Comparison of computed and measured wing tip bending and twist deformation over angle-of-attack.

Summary & Conclusions

DLR's results from the seventh AIAA Computational Fluid Dynamics Drag Prediction Workshop, obtained at the Institute of Aerodynamics and Flow Technology, are presented. The effects of spatial discretization and turbulence modelling at transonic flow conditions and in the vicinity of shock-induced separation were investigated during this workshop.

For the CFD simulations a family of six grids, ranging in size from 11.7 to 165 million points, were generated on the CRM Wing-Body configuration using the commercial grid generation package SOLAR for hex-dominant meshes. Additionally, a grid series with the wing deformed for eight angles-of-attack was built.

The grid convergence study revealed an almost linear variation of overall aerodynamic coefficients with grid size, which is in good agreement to the Richardson extrapolation for 2^{nd} order codes. The influence of both grid size and turbulence model was found to be very small. Wing static pressure distributions show an upstream movement of shock location on the outboard wing, both with increasing mesh size and from SA-neg to RSM-ln(ω). The side-of-body flow separation grows with grid size and from RSM-ln(ω) to SA-neg.

In the angle-of-attack sweep CFD solutions show higher lift and a more negative pitching moment compared to the wind tunnel results. To some extent the deviations could be caused by the missing mounting system corrections in the experimental data, and by the model suspension not being included in the CFD geometry. With the SA-neg turbulence model the sudden development of a side-of-body separation is observed at $\alpha = 4.00°$. The stronger pitch break in the RSM-ln(ω) model results is associated with a larger upstream shock movement with increasing angle-of-attack compared to SA-neg.

Reynolds number increments correctly capture the expected gain in lift with increased Reynolds number. Because of the benign flight condition without flow separations the differences between the investigated turbulence models remain small. The correlation to ETW data corrected for sting effects was found to be better than for NTF.

In the aeroelastic simulation test case a good agreement of pressure distributions and wing bending and twist deformations to experimental data was found. Results from the angle-of-attack sweep show that DLR's aeroelastic simulation approach accurately predicts aerodynamic performance parameters and wing deformations for varying aerodynamic loads.

Acknowledgments

Experimental data from NTF was made available by NASA on the CRM website. ETW data was provided through the European research project ESWI^{RP} (European Strategic Wind tunnels Improved Research Potential)[6]. The authors wish to thank the DPW Organizing Committee for the excellent collaboration.

4. Contact Author Email Address

For any correspondence regarding this paper please contact: Stefan.Keye@dlr.de.

5. Copyright Statement

References

[1] K. Becker and J. Vassberg. Numerical Aerodynamics in Transport Aircraft Design. In E.-H. Hirschel and E. Krause, editors, *Notes on Numerical Fluid Mechanics and Multidisciplinary Design*, volume 100, pages 209–220. Springer, 2009.

[2] C.-C. Rossow and L. Cambier. European Numerical Aerodynamics Simulation Systems. In E.-H. Hirschel and E. Krause, editors, *Notes on Numerical Fluid Mechanics and Multidisciplinary Design*, volume 100, pages 189–208. Springer, 2009.

[3] D. Levy, T. Zickuhr, J. Vassberg, S. Agrawal, R. Wahls, S. Pirzadeh, and M. Hemsch. Summary of data from the first aiaa cfd drag prediction workshop. AIAA Paper 2002–0841, January 2002.

[4] K. Laflin, S. Klausmeyer, T. Zickuhr, J. Vassberg, R. Wahls, J. Morrison, O. Brodersen, M. Rakowitz, E. Tinoco, and J.-L. Godard. Data summary from second aiaa computational fluid dynamics drag prediction workshop. *AIAA Journal of Aircraft*. Vol. 42, No. 5, 2005, pp. 1165–1178.

[5] J. Vassberg, E. Tinoco, M. Mani, O. Brodersen, B. Eisfeld, R. Wahls, J. Morrison, T. Zickuhr, K. Laflin, and D. Mavriplis. Abridged Summary of the Third AIAA Computational Fluid Dynamics Drag Prediction Workshop. *AIAA Journal of Aircraft*. Vol. 45, No. 3, pp. 781-798, 2008.

[6] J. Vassberg, E. Tinoco, M. Mani, T. Zickuhr, D. Levy, O. Brodersen, S. Crippa, R. Wahls, J. Morrison, D. Mavriplis, and M. Murayama. Summary of the Fourth AIAA Drag Prediction Workshop. Paper 2010–4547, AIAA, June 2010.

[7] D. Levy, K. Laflin, E. Tinoco, J. Vassberg, M. Mani, B. Rider, C. Rumsey, R. Wahls, J. Morrison, O. Brodersen, S. Crippa, D. Mavriplis, and M. Murayama. Summary of data from the fifth aiaa cfd drag prediction workshop. Technical report. Vol. 51, No. 4, pp. 1194–1213, 2014.

[8] Christopher J. Roy, Christopher L. Rumsey, and Edward N. Tinoco. Summary data from the sixth aiaa computational fluid dynamics drag prediction workshop: Code verification. *Journal of Aircraft*, 2018.

[9] Edward N. Tinoco, Olaf Brodersen, Stefan Keye, Kelly R. Laflin, Edward J. Feltrop, John C. Vassberg, M. Mani, Ben Rider, Richard A. Wahls, Joseph H. Morrison, David Hue, Christopher J. Roy, Dimitri J. Mavriplis, and Mitsuhiro Murayama. Summary data from the sixth aiaa cfd drag prediction workshop: Crm cases. *Journal of Aircraft*, 2017.

[10] Stefan Keye, Martin Sitzmann, Olaf Brodersen, and Ralf Heinrich. Fluid-structure coupled loads analysis of dlr's f6 wing-body configuration. Number 2008–0675, January 2008.

[11] S. Keye, O. Brodersen, and M. Rivers. Investigation of aero-elastic effects on the dlr results of the fifth aiaa drag prediction workshop. *AIAA Journal of Aircraft*, 2014. Vol. 51, No. 4, 2014, pp. 1323–1330.

[12] Stefan Keye and Mark Gammon. Development of deformed cad geometries of nasa's common research model for the 6th aiaa cfd drag prediction workshop. Number 2016–3431, January 2016.

[13] P. Wegener and S. Keye. Cad deformation for the consideration of aeroelastic effects. 33rd Congress of the International Council of the Aeronautical Sciences ICAS2022, Sept. 2022.

[14] M. Rakowitz, M. Sutcliffe, B. Eisfeld, D. Schwamborn, H. Bleeke, and J. Fassbender. Structured and unstructured computations on the dlr–f4 wing–body configuration. Paper 2002-0837, AIAA, 2002.

[6] http://www.eswirp.aero/

[15] O. Brodersen, M. Rakowitz, S. Amant, P. Larrieu, D. Destarac, and M. Sutcliffe. Airbus, ONERA, and DLR Results from the Second AIAA Drag Prediction Workshop. *AIAA Journal of Aircraft*. Vol. 42, No. 4, pp. 932–940, 2005.

[16] O. Brodersen, B. Eisfeld, J. Raddatz, and P. Frohnapfel. DLR Results from the Third AIAA CFD Drag Prediction Workshop. *AIAA Journal of Aircraft*. Vol. 45, No. 3, pp. 823–836, 2008.

[17] O. Brodersen, S. Crippa, B. Eisfeld, S. Keye, and S. Geisbauer. DLR Results from the Fourth AIAA CFD Drag Prediction Workshop. AIAA Paper 2010–4223, June 2010.

[18] O. Brodersen and S. Crippa. RANS-based Aerodynamic Drag and Pitching Moment Predictions for the Common Research Model. 124:485–493, 2014. DGLR STAB Workshop 2012.

[19] S. Keye, V. Togiti, B. Eisfeld, O. Brodersen, and M.B. Rivers. Investigation of Fluid-Structure-Coupling and Turbulence Model Effects on the DLR Results of the Fifth AIAA CFD Drag Prediction Workshop. AIAA Paper 2013–2509, AIAA, June 2013.

[20] S. Keye, V. Togiti, and O. Brodersen. DLR Results of the Sixth AIAA Computational Fluid Dynamics Drag Prediction Workshop. AIAA Paper 2017–4232, AIAA, June 2017.

[21] Stefan Keye, Olaf Brodersen, Stefan Melber-Wilkending, Diliana Friedewald, and Michael Fehrs. Dlr results of the seventh aiaa computational fluid dynamics drag prediction workshop. Number 2023–4120, June 2023.

[22] J. Vassberg, M. DeHaan, S. Rivers, and R. Wahls. Development of a Common Research Model for Applied CFD Validation Studies. Paper 2008–6919, AIAA, June 2008.

[23] S. Keye, O. Brodersen, and M.B. Rivers. Investigation of aeroelastic effects on the nasa common research model. *AIAA Journal of Aircraft*, 2014. Vol. 51, No. 4, 2014, pp. 1323–1330.

[24] European Commission (EU). European strategic wind tunnels improved research potential. In [online web site], http://www.eswirp.aero/. 2015.

[25] D. Martineau, S. Stokes, S. Munday, A. Jackson, B. Gribben, and N. Verhoeven. Anisotropic hybrid mesh generation for industrial rans applications. AIAA Paper 2006-0534, January 2006.

[26] M. Galle. Ein Verfahren zur numerischen Simulation kompressibler, reibungsbehafteter Strömungen auf hybriden Netzen. Phd thesis, Uni Stuttgart, 1999.

[27] N. Kroll, C.-C. Rossow, K. Becker, and F. Thiele. MEGAFLOW – A Numerical Flow Simulation System. *Aerospace Science Technology*. Vol. 4, 2000, pp. 223–237.

[28] T. Gerhold. Overview of the Hybrid RANS Code TAU. In N. Kroll and J. Fassbender, editors, *MEGAFLOW*, volume 89 of *Notes on Numerical Fluid Mechanics and Multidisciplinary Design*, pages 81–92. Springer, 2005.

[29] A. Jameson, W. Schmidt, and E. Turkel. Numerical solution of the euler equations by finite volume methods using runge–kutta time stepping schemes. AIAA Paper 81–1259, January 1981.

[30] R. C. Swanson and E. Turkel. On Central Differences and Upwind Schemes. *Journal of Computational Physics*. Vol. 101, pp., 1992.

[31] S. R. Allmaras, F. T. Johnson, and P. R. Spalart. Modifications and Clarifications for the Implementation of the Spalart-Allmaras Turbulence Model. 7th International Conference on Computational Fluid Dynamics, ICCFD7-1902, Big Island, Hawaii, 2012.

[32] P.R. Spalart. Strategies for turbulence modelling and simulations. Technical report. Vol. 21, pp. 252-263, 2000.

[33] B. Eisfeld and C. Rumsey. Length-Scale Correction for Reynolds-Stress Modeling. *AIAA Journal of Aircraft*. Vol. 58, No. 4, pp. 1518–1528, 2020.

[34] R. Heinrich, J. Wild, T. Streit, and B. Nagel. Steady fluid-structure coupling for transport aircraft. ONERA-DLR Aerospace Symposium, Oct. 2006.

[35] MSC Software Corporation. Product information. In [online web site], https://www.mscsoftware.com/product/msc-nastran/. 2013.

[36] S. Keye and R. Rudnik. Aero-elastic simulation of dlr's f6 transport aircraft configuration and comparison to experimental data. AIAA Paper 2009–0580, AIAA, January 2009.

[37] S. Keye and R. Rudnik. Validation of Wing Deformation Simulations for the NASA CRM Model using Fluid-Structure Interaction Computations. AIAA Paper 2015–0619, AIAA, January 2015.

[38] S. Keye and R. Rudnik. Validation and Assessment of Turbulence Model Impact for Fluid-Structure Coupled Computations of the NASA CRM. 5th CEAS Air & Space Conference, Paper no. 103, CEAS, September 2015.

[39] S. Keye. Fluid-structure coupled analysis of a transport aircraft and flight-test validation. *AIAA Journal of Aircraft*, 2011. Vol. 48, No. 2, 2011, pp. 381–390.

[40] S. Keye. An Assessment of the Influence of Fuselage Deformations on the Numerical Prediction of High-Lift Performance. 124:385–393, 2014. DGLR STAB Workshop 2012.

[41] D. Rohlmann and S. Keye. Stall Maneuver Simulation of an elastic Transport Aircraft based on Flight Test Data. AIAA Paper 2015–2570, AIAA, June 2015.

[42] S. Keye and D. Rohlmann. Aeroelastic Effects in Maximum Lift Prediction of a Transport Aircraft and Comparison to Flight Data. AIAA Paper 2014–2842, AIAA, June 2014.